Mechanical and thermal properties of grain boundary in a planar heterostructure of graphene and hexagonal boron nitride

Yinfeng Li[a,b,*], Anran Wei [a], Han Ye[c], Haimin Yao[d]

a. Department of Engineering Mechanics, School of Naval Architecture, Ocean and Civil Engineering (State Key Laboratory of Ocean Engineering), Shanghai Jiao Tong University, Shanghai 200240, China

b. Collaborative Innovation Center for Advanced Ship and Deep-Sea Exploration, Shanghai 200240, China

c. State Key Laboratory of Information Photonics and Optical Communications, Beijing University of Posts and Telecommunications, Beijing 100876, China

d. Department of Mechanical Engineering, The Hong Kong Polytechnic University, Hong Kong, China

Abstract In this paper, the mechanical properties of grain boundaries (GBs) in planar heterostructures of graphene and hexagonal Boron Nitride (h-BN) are studied with molecular dynamics method in combination with classical disclination theory. The hybrid interface between graphene and h-BN grains is optimally matched by non-bisector GB composed of pentagon-heptagon defects arranged in a periodic manner. GB is found a vulnerable spot where failure initiates under uniaxial tension, and the tensile strength is found to anomalously increase with the mismatch angle between graphene and h-BN grains, i.e., the density of pentagon-heptagon defects along GBs. The disclination theory is successfully adopted to predict the stress field caused by the lattice mismatch at GB. Comparison between stress contours of GBs with different mismatch angle demonstrates that the arrangement of 5-7 disclinations along GB is crucial to the strength, and the stress concentration at GB decreases with the increase of disclination density, resulting in the anomalous increase of strength with mismatch angle of grains. What's more, the thermal transfer efficiency of hybrid GB is also revealed to depend not only on the mismatch angle of grains but also the direction of thermal flux. Thermal transfer efficiency from graphene to h-BN is higher than that from h-BN to graphene. Detailed analyses for the phonon density of states (PDOS) of GB atoms are carried out for the mismatch angle-dependence of interfacial conductance. Our results provide useful insights into the application of two dimensional polycrystalline heterostructures for next-generation electronic nanodevices.

Keywords: Heterostructure, graphene, hexagonal Boron Nitride, molecular dynamics, disclination theory.

* Corresponding author. Electronic addresses: liyinfeng@sjtu.edu.cn (Y. Li)

Introduction

Two-dimensional (2D) materials have been remarkably investigated for their exceptional properties, while the hybridization of different single-atomic materials in one plane is of special interest since it can provide unique flexibilities in tuning the properties[1]. Graphene and hexagonal boron-nitride (h-BN) sheets are the two most widely studied 2D materials consisting of a single layer of hexagonally arranged atoms while exhibiting distinctive and distinguished properties.[2-5] Their least lattice mismatch makes them be the best candidates to be heterogeneously integrated for tunable properties. For example, graphene has a major problem for novel 2D semiconductor applications as it lacks an energy gap between its conduction and valence bands[6] while the h-BN is electrically insulative with a band gap of ~5.8 eV [7-9]. The hybridization of these two 2D materials provides unique tunable electrical properties spanning from semiconducting to half-metallic as the ratio of composition varies[10, 11]. Compared to the surface functionalized graphene or BN nanosheets with similar tunable properties[12], in-plane graphene-BN hybridization is far more appealing as the single-atomic thickness is maintained. Studies focusing on the modulations of magnetic[13, 14], electrical[15], thermal [16] and mechanical [17, 18] properties of hybrid CBN sheet by changing the hybrid configurations have been reported. More interesting physical and chemical properties are expected in the CBN in-plane heterostructure.

Recent advances in the fabrication of in-plane heterostructure composed of graphene and h-BN domains provide strong evidence for its potential application in next generation electronic devices [19-21]. Nearly seamless BNC hybrid films can be generated under ultra-high vacuum (UHV) conditions via a two-step heteroepitaxial growth method [22, 23]. BNC hybrid planar heterostructures with controlled domains ranging from tens of nanometers to millimeters has also

been successfully generated using a two-step patching growth approach [24]. The fabrication achievements have paved an avenue in realizing precise spatial control over the electrical properties of the BNC hybrid nanosheets[19]. Chemical Vapor Deposition is an integral fabrication process [25-27] for the production of hybrid graphene-BN nanosheets in all the reported experiments. Thus, the formation of grain boundaries (GBs) where two grains meet each other are unavoidable during the CVD method because each grain in metallic substrate could be a nucleation site for individual grains of nanosheets [28-30]. Most recent transmission electron microscope study of CVD grown 2D nanomaterials with hexagonal lattices find that GBs are mainly consisting of pentagon–heptagon (5-7) defects [31]. Such topological defects at GB may act as dislocation cores that raise stress concentration, consequently the physical and chemical properties of nanomaterials are altered [32-36]. Detailed theoretical and simulation analysis demonstrates that the strength of graphene with bisector GBs consisting of 5-7 defects can either increase or decrease with the mismatch angle, depending on the arrangements of the 5-7 defects.[36, 37]

The interface between graphene and h-BN domain has been demonstrated to govern the failure mechanism of the hybrid sheet by molecular dynamic simulations[38], while a little mixing of h-BN and graphene can cause noticeable drop in the strength of the hybrid sheet.[39] The mechanical and failure behaviors of the hybrid CBN nanosheets are also noticed to be affected by the type of interface connection and the type of defects by density functional theory.[40] Thus, a fundamental understanding to the role of interfaces between graphene and h-BN grains in the mechanical, thermal, and electronic properties of CBN heterostructure is a key for fabricating high-performance nanoarchitectures.[39] Recently, a pioneering effort about the GBs in hybrid 2D nanosheets revealed that two heterogeneous domains in hybrid graphene-BN

nanosheet tend to optimally match by forming bisector GB composed of 5-7 pairs arranged in a periodic manner. Such GB is different from the bisector GB in pristine graphene or h-BN due to the lattice mismatch between the heterogeneous domains.[41] Moreover, experimental study found that GBs with periodic 5-7 pairs in quasi-freestanding graphene give sharp local density of states (LDOS) peaks as opposed to the broad peaks of the aperiodic boundaries, which suggests that GBs with high structural quality can introduce well-defined electronic states.[42] Thus, study of the effect of non-bisector GB on the mechanical, thermal, and electronic properties of CBN heterostructure is highly demanded. To this aim, we study the effect of non-bisector GBs on the mechanical and thermal properties of hybrid graphene-BN combining molecular dynamics simulations and disclination theory. Our results reveal that the existence of GBs in graphene/h-BN heterostructure can result in noticeable change in both mechanical and thermal properties. By increasing the density of 5-7 defects in the non-bisector GBs, the strength of the planar heterostructure increases while the thermal conductivity decreases gradually. Both the influences of GBs on the mechanical and thermal properties can be attributed to the arrangement of 5-7 defects at GB. Our results suggest that the effect of GB on the mechanical and thermal properties of hybrid CBN nanosheet should be considered carefully when evaluating its whole performance in bandgap-engineered applications such as electronics and optics.

Simulation methodology

We use the Tersoff potential with parameters adopted from Kınacı *et al.*[43] in LAMMPS[44] package for MD simulations. The size of the hybrid BNC models used in simulations is approximately 8nn×8nm (Fig. S1*a*). Non-bisector GB defects are placed in the middle of these heterostructures along *y*-direction. GBs of different mismatch angles are constructed as shown in

Fig. 1*a*. All the atom models are fully relaxed by energy minimization before applying uniaxial tensile strain along *x*-direction. A 3Å wide ribbon at each end of the hybrid sheet along *x*-direction is fixed by specifying the velocity and the force of atoms equal to zero along *x*- and *z*-direction, as depicted by the pink arrows in Fig. S1*a*. With these constraints, the hybrid sheet is stretched along *x*-direction at a strain rate of 0.01%/ps by scaling all atomic coordinates. Each stretching step is followed by a relaxation of 100 steps. Such procedure of stretching and relaxation is repeated at time step τ = 1 fs until complete failure. All sets of MD simulations are performed at room temperature under NVE ensemble.

To obtain the stress-strain curves during deformation, the atomic stress of individual atoms in the hybrid sheet is calculated according to equation [45, 46]

$$\sigma^{\alpha}{}_{ij} = \frac{1}{\Omega^{\alpha}}\left(\frac{1}{2} m^{\alpha} v_i^{\alpha} v_j^{\alpha} + \sum_{\beta=1,n} r_{\alpha\beta}^{j} f_{\alpha\beta}^{i}\right) \quad (1)$$

where i and j denote indices in Cartesian systems; α and β are the atomic indices; m^{α} and v^{α} denote the mass and velocity of atom α; $r_{\alpha\beta}$ is the distance between atoms α and β; Ω^{α} is the atomic volume of atom α. After obtaining the stress of each atom, the stress of the hybrid BNC sheet is computed by averaging over all the atoms in the sheet. The thickness of hybrid graphene–BN sheet is adopted as 3.35 Å[17], which is the mean thickness of graphene and BN. The Young's modulus E is calculated as the initial slope of the stress-strain curve and the ultimate strength σ is taken as the peak stress of the curve.

Thermal properties of hybrid CBN sheets are investigated using non-equilibrium molecular dynamics (NEMD) method, which key idea is to apply a heat flux across the system and obtain the temperature profile along the direction of heat flux to determine the temperature gradient. Figure 5*a* shows the illustration of the NEMD simulation for the thermal properties of hybrid GB in planar graphene/h-BN heterostructures. The overall simulation length along *x*-direction

includes the fixed boundary, hot and cold slabs and free domains. The atoms within a width of 3Å at each end of the hybrid sheet are fixed after energy minimization to prevent the system from drifting and oscillating. With these constraints in place, the heterostructure is relaxed for equilibrium at room temperature (300 K) under NVT ensemble for 10 ns with time step τ = 0.1 fs. To obtain the temperature profile in graphene, we divide the unfixed domain into 10 narrow slabs equally along *x*-direction, where the first slab and the last slab correspond to the hot and cold domains. The average temperatures in hot and cold slab are set to be $T_{\text{hot}} = 320K$ and $T_{\text{cold}} = 280K$, respectively. Heat flux occurs from hot slab to cold slab along *x*-direction. The heat flux *J* is defined as the energy transported across the simulation system per unit cross-sectional area and unit time, which can be expressed as

$$J = \frac{1}{V}\left[\sum_{i}^{N}\varepsilon_i v_i + \frac{1}{2}\sum_{ij;j\neq j}^{N}(F_{ij}\cdot v_i)r_{ji} + \frac{1}{6}\sum_{jik;i\neq j\neq k}^{N}(F_{ijk}\cdot v_i)(r_{ji}+r_{ik})\right] \tag{2}$$

where the subscripts *i*, *j*, *k* denote the three different atoms *i*, *j*, *k*. ε_i and v_i are the energy and velocity of atom *i*, respectively. Vector r_{ij} represents the interatomic distance between atoms *i* and *j*, and F_{ij} and F_{ijk} represent the two-body and three-body forces, respectively. *V* is the volume of the studied system. After a simulation period of 5 ns, a dynamic equilibrium state of heat flux transport across the nanosheet can be reached. Figure 5*b* plots the evolution of total energy transported across the nanosheet per unit cross-sectional area over simulation time. Such linear increase of total energy with simulation time suggests a steady and time-independent heat flux *J*. The averaged heat flux *J* is calculated from the slope of the curve. The temperature profile along nanosheet can be established by the temperature in each slab, which is determined by[47]:

$$T_{slab} = \frac{2}{3Mk_B}\sum_{j}\frac{p_j^{\,2}}{2m_j}. \tag{3}$$

In Eq. (3), M is the number of atoms in the slab, m_j and p_j represent the mass and momentum of atom j respectively, and k_B is the Boltzmann constant. The temperature gradient dT / dx is calculated from the linear fit of the temperature in each slab.

Results and discussions

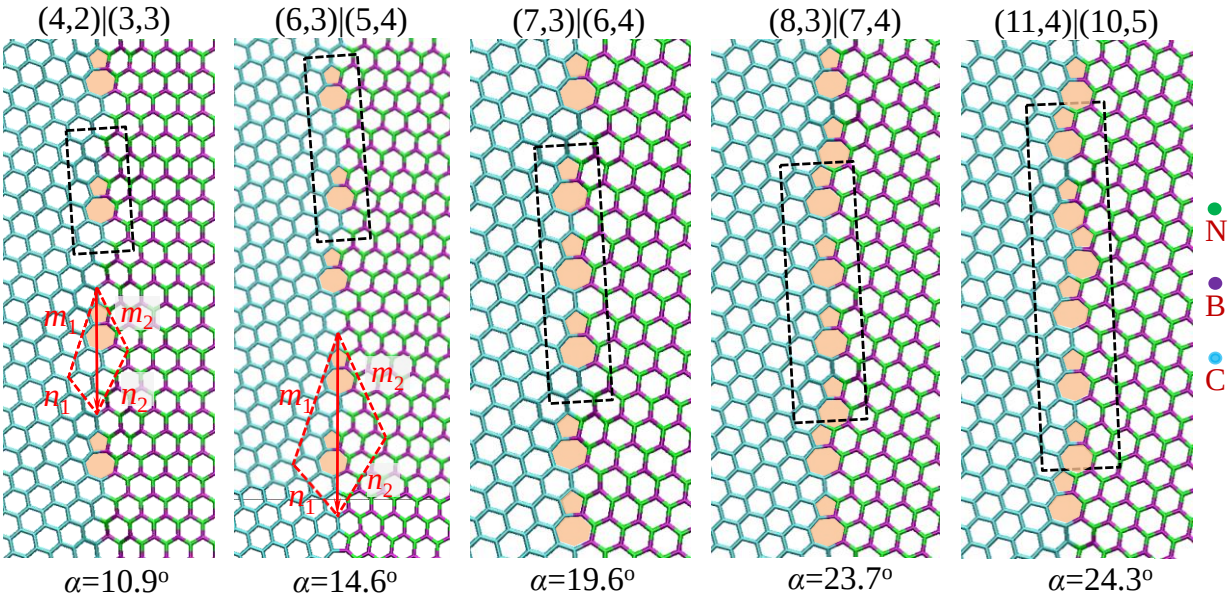

Fig.1 Atomistic structures of the optimal match between graphene and h-BN grains in polycrystalline heterostructures of graphene and hexagonal boron nitride. The GB is composed of hybrid CBN pentagon-heptagon dislocations arranged in a periodic manner. The black box marks one unit cell of the GB. The chirality of graphene and h-BN grains are featured by (m_1, n_1) and (m_2, n_2) as illustrated by the red lines. The angles of mismatch between graphene and h-BN grains are α = 10.9°, 14.6°, 19.6°, 23.7°, 24.3°, respectively.

GBs connecting the heterogeneous grains in hybrid graphene and h-BN nanosheets have been proposed to obey the light refraction theorem, where the ratio of cosines of the rotation angles of graphene and h-BN should be equivalent to the ratio of the lattice constants of two components[41]. Such non-bisector GB composed of 5-7 defects has been demonstrated as an optimal match between heterogeneous grains with minimal intrinsic strain and well-defined

electronic states in both theoretical and experimental studies.[42, 48]. In this paper, five armchair-oriented CBN heterostructures with optimal asymmetric GBs are constructed as shown in Fig.1. Compared to the straight symmetric GBs in pure polycrystalline graphene, GBs here are composed of periodically arranged 5-7 pairs or a sequence of 5-7 clusters which are deviated from the vertical. The rotation angles of graphene and h-BN grains connected by the asymmetric GB differ. The angle of 5-7 pair deviating from vertical $\Delta\theta$ is half of the angle of mismatch between graphene and h-BN grains α. The rotation angles of the graphene and h-BN domains along GBs are defined by vectors (m_1, n_1) and (m_2, n_2) respectively. Thus, the five non-bisector GBs in Fig.1 can be represented by chirality $(m_1, n_1)|(m_2, n_2)$, namely (4,2)|(3,3), (6,3)|(5,4), (7,3)|(6,4), (8,3)|(7,4), and (11,4)|(10,5). The corresponding angles of mismatch between graphene and h-BN grains connected by these five GBs are $\alpha = 10.9^o, 14.6^o, 19.6^o, 23.7^o, 24.3^o$.

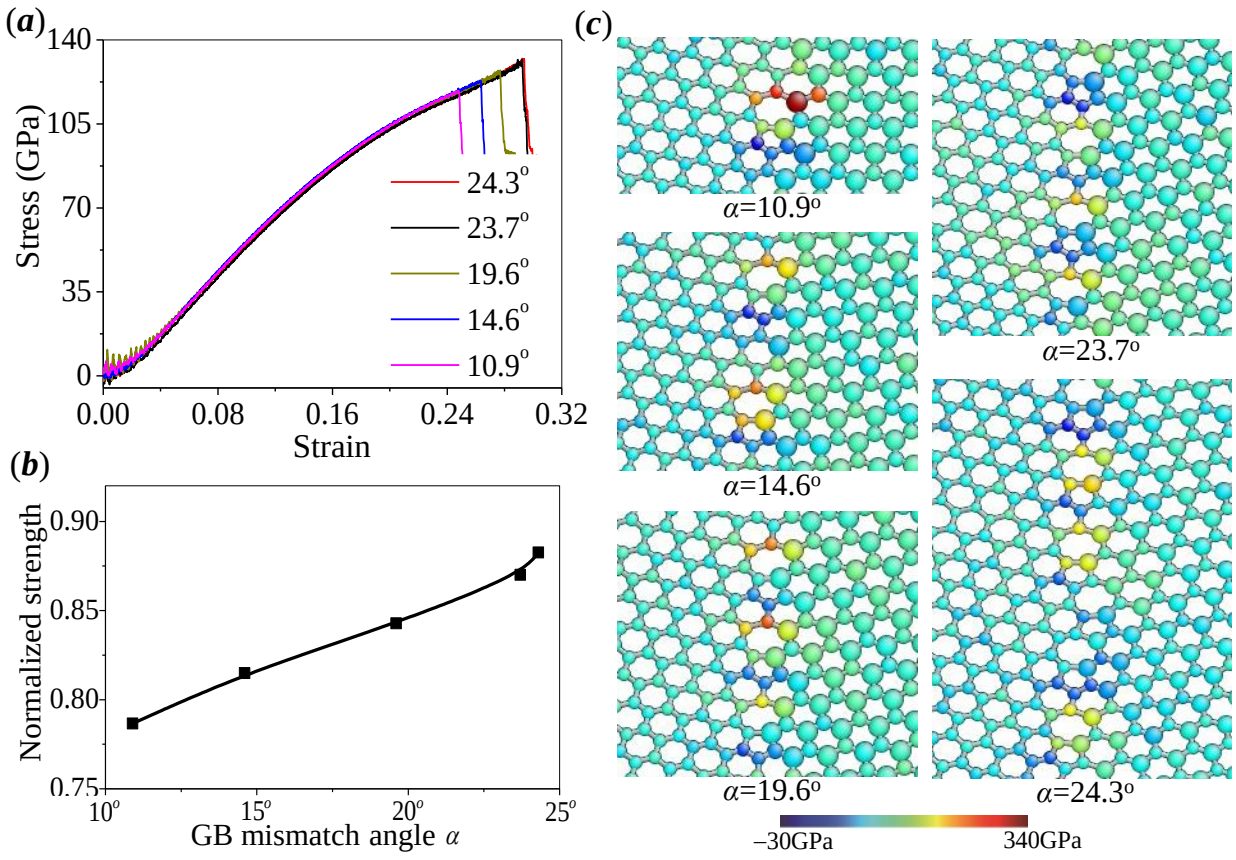

Fig. 2 Comparisons between mechanical characteristics of planar graphene/h-BN heterostructure embedded with asymmetric GBs of different angles under uniaxial tension perpendicular to GB. (*a*) The stress-strain curves of hybrid CBN nanosheet with GB of different mismatch angles. (*b*) Evolution of ultimate strength with the mismatch angle between graphene and h-BN grains. (*c*) Comparison of stress contours of σ_x between hybrid nanosheets under the same strain.

Molecular dynamics simulation is adopted to examine the mechanical properties of these heterostructures under uniaxial tension. In these simulations, periodic boundary conditions are applied on the upper and bottom edges of the nanosheet while pulling is applied on the left and right ends until complete failure (Fig. S1). The stress-strain curves are recorded as shown in Fig. 2*a*. The Young's modulus is insensitive to the change of GBs while the ultimate strength and failure strain show strong dependency on the angle of mismatch α. In order to investigate the dependency of mechanical strength on GB, we plot the normal tensile strength as a function of the mismatch angles as shown in Fig. 2*b*. The strengths are normalized by the calculated tensile strength of pristine graphene for qualitative discussion. The normal tensile strength of heterostructure increases monotonically with the angle of mismatch between graphene and h-BN grains. Such positive correlation between the mismatch angle and normal strength implies an effective and convenient method to manipulate the mechanical properties of hybrid nanosheets.

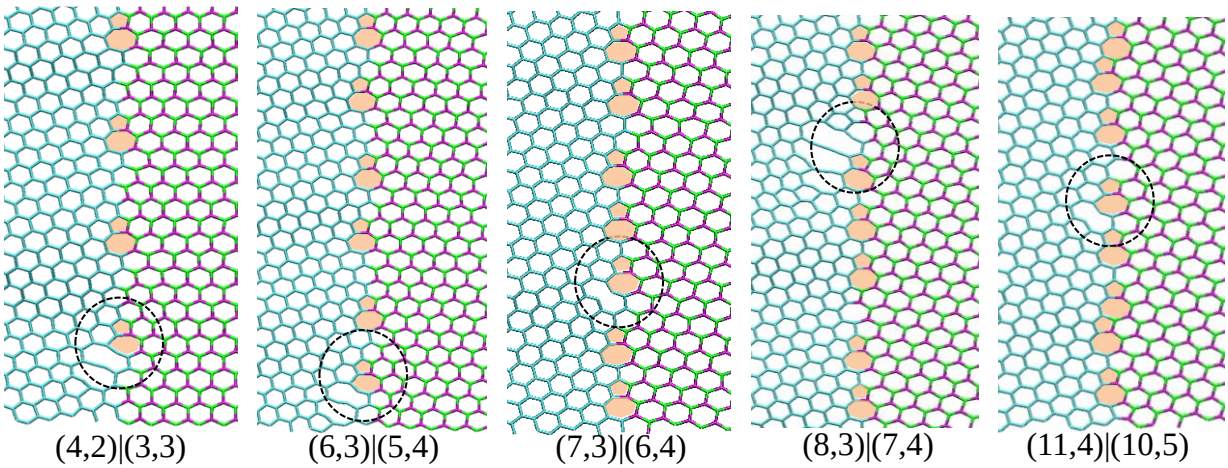

Fig. 3. Snapshots taken from MD simulations at the onset of failure initiation in heterostructures under horizontal pulling.

By studying the dynamic failure under uniaxial tension, it is observed that the failure process always initiates from the GB and then propagation of crack leads to the ultimate failure of nanosheet. Figure 3 shows the snapshots taken at the onset of failure initiation (The dynamic failure process can be referred to Video S1-2). The failure process initiates from the bottom most 5-7 defects in the bottom most cluster of GB (6,3)|(5,4) and GB (8,3)|(7,4) GB while the failure initiates from the upmost 5-7 defects in the cluster of GB (7,3)|(6,4) and GB (11,4)|(10,5) (Pentagon down and heptagon up). Such failure mode reveals that GB, where failure initiates, is the most vulnerable venue under tension. The strength of the optimal match between graphene and h-BN grains can be analyzed from the perspective of stress distribution. Figure 2*c* shows the stress contours of σ_x in a unit cell of the GB with different mismatch angles under given strain $\varepsilon = 0.2$. For these heterostructures, the stress distribution at 5-7 defects shows a similar polar nature as that of the 5-7 defects in pristine GB as reported by Wei *et al*[37]. The strength of CBN nanosheet under uniaxial tension along *x*-direction is governed by the peak value of stress component σ_{xx} at GB where stress concentrations appear. The degree of stress concentration at GBs decreases gradually with the increases of mismatch angle α due to the mutual interactions between the polarized stress fields of 5-7 defects. As a result, the normal strength of GBs increases with the mismatch angle θ.

In order to further verify the MD simulation results as well as the mechanism of the monotonic increase of strength with mismatch angle, we adopted the classical disclination theory for the stress field at the 5-7 defects of non-bisector GB. The disclination model has been applied to explain the relationship between the strengths of GBs in graphene and the mismatch angles, as well as the boundary structures in silicon, germanium, biomaterials and fullerenes.[37, 49] Based on the continuum mechanics, the strain component ε_y in graphene and h-BN domains under

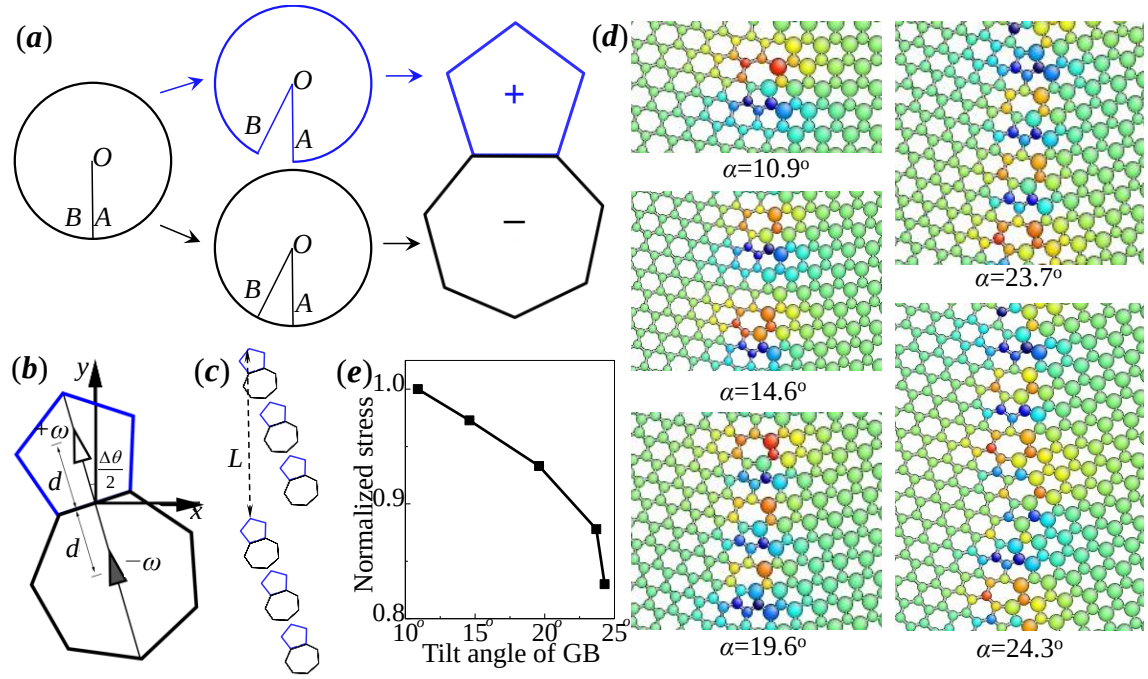

Fig. 4. The stress field of 5-7 defects in asymmetric GBs based on disclination theory. (***a***) 5-7 pair can be treated as a pair of positive and negative disclinations. (***b***-***c***) The Cartesian system for the deviated 5-7 pair and 5-7 clusters in asymmetric GB. (***d***-***e***) show the distribution of intrinsic stress σ_{xx} at 5-7 defects in a unit periodic of GB, and the evolution of the normalized peak stress in these contours with the mismatch angle of GB.

tension along *x*-direction can be expressed as:

$$\varepsilon_{yG} = \sigma_{yG} / E_G - \nu_G \sigma_x$$
$$\varepsilon_{yBN} = \sigma_{yBN} / E_{BN} - \nu_{BN} \sigma_x \tag{5}$$

where σ_x is the tensile stress along the direction of loading, E_G and E_{BN} are Young's modulus of graphene while ν_G , ν_{BN} represent Passion's ratios. Since the nanosheets has periodic boundary conditions along *y*-direction, the strain components ε_y in graphene and h-BN domains equals zero, *i.e.*, $\varepsilon_{yG} = \varepsilon_{yBN} = 0$. Thus, we have:

$$\sigma_{yG} = \nu_G \sigma_x, \sigma_{yBN} = \nu_{BN} \sigma_x \tag{6}$$

which implies that the lattice mismatch only causes different normal stress in *y*-direction. The normal stress along *x* direction is still uniform in the heterostructure. Thus, we adopt the classical disclination theory to estimate the distribution of residual stress σ_x , which is crucial to the strength of the nanosheet. Based on the disclination theory, the elastic stress field induced by a positive wedge disclination residing at (0, y_0) is expressed as[50]:

$$\sigma_x = \frac{\omega E}{4\pi}[\ln r + \frac{(y-y_0)^2}{r^2} + \frac{1}{2}] \tag{4}$$

where *E* is the Young's modulus, ω is the rotational strength of the wedge disclination. From a geometrical perspective, a pentagon-heptagon defect resembles a disclination dipole where the pentagon ring corresponds to a positive wedge disclination while the heptagon ring represents a negative wedge disclination (Fig.4*a*). Building a Cartesian coordinate system at the center of the critical pentagon-heptagon bond, the elastic fields of a disclination dipole with a positive disclination residing at (x_1, y_1) and a negative one at (x_2, y_2) can be expressed as [37, 51]

$$\sigma_x(x, y, x_1, y_1, x_2, y_2) = \frac{\omega E}{4\pi}[\ln \frac{r_1}{r_2} + \frac{(y-y_1)^2}{r_1^2} - \frac{(y-y_2)^2}{r_2^2}] \tag{5}$$

where $r_1^2 = (x-x_1)^2 + (y-y_1)^2$, $r_2^2 = (x-x_2)^2 + (y-y_2)^2$. As shown in Fig 4*b*, we use *d* to represent the half-distance between the centers of positive disclination and negative disclination, $\Delta\theta$ is the oblique angle of a disclination dipole which equals half of the angle of mismatch between graphene and h-BN grains. Then, we have

$$x_1 = -d\sin\Delta\theta\,,\ y_1 = d\sin\Delta\theta\,,\ x_2 = d\sin\Delta\theta\,,\ y_2 = -d\sin\Delta\theta\,. \tag{6}$$

The stress distribution of GB residual stress is the superposition of the stress fields of 5-7 defects along the GB. For asymmetric GB composed of an array of disclination dipole clusters which are evenly spaced by a periodicity *L*, the total normal stress at (x, y) can be expressed as

$$\sigma_x = \sum_{k=-\infty}^{+\infty} \sum_{n=1}^{m} \sigma_x(x, y, x_{n1}, y_{n1} + kL, x_{n2}, y_{n2} + kL) \tag{7}$$

where m represents the number of disclination dipoles in each cluster, (x_{n1}, y_{n1}) and (x_{n2}, y_{n2}) are the coordinates of the nth positive and negative disclination in each cluster. Fig. 4*c* gives an example of GB with 3 disclination dipoles in one cluster. Here, we choose the cutoff range for the infinite summation in Eq. 7 as $-30 \le k \le 30$ for numerical calculation. The change of the numerical results is negligible when $|k| > 30$. Eq. 7 gives the expression of the residual stress σ_x caused by the lattice mismatch at GB in a flattened heterostructure. Since the out-of-plane corrugations of GBs can be suppressed by uniaxial tension, the ultimate strength of heterostructure can be reflected from the degree of stress concentration calculated from Eq. 7.

Figure 4*d* plots the contours of residual stress σ_x in one unit cell of asymmetric GB. The stress values are converted into dimensionless quantities by dividing $\omega E / 4\pi$ for each GB. We can see that the theoretical stress field is polarized at the defected regions which are similar to the contours calculated from MD simulations. In addition, we find that the theoretical position of the maximum normal tensile stress in one cluster is also consistent with the MD results as plotted in Fig. 2. The stress distribution becomes more uniform with the increase of mismatch angle of GB. Fig. 4*e* shows the comparison between the maximum stresses in these contours as a function of the mismatch angle α. The maximum stresses are normalized by the maximum stress in the contour of (4,2)|(3,3) GB. It can be seen that the residual stress in relaxed asymmetric GBs decrease monotonically with the increase of mismatch angle between graphene and h-BN grains. The asymmetric GBs with smaller intrinsic stress correspond to a higher tensile strength. Such trend indicates that the stress distribution in GBs of large mismatch angle is more uniform than that of GBs with smaller mismatch angle under the same strain. The stress distribution is

sensitive to the density as well as the arrangement of 5-7 defects along GB. Such trend is different from the evolution of GB strength with the mismatch angle between two adjacent homogeneous grains.

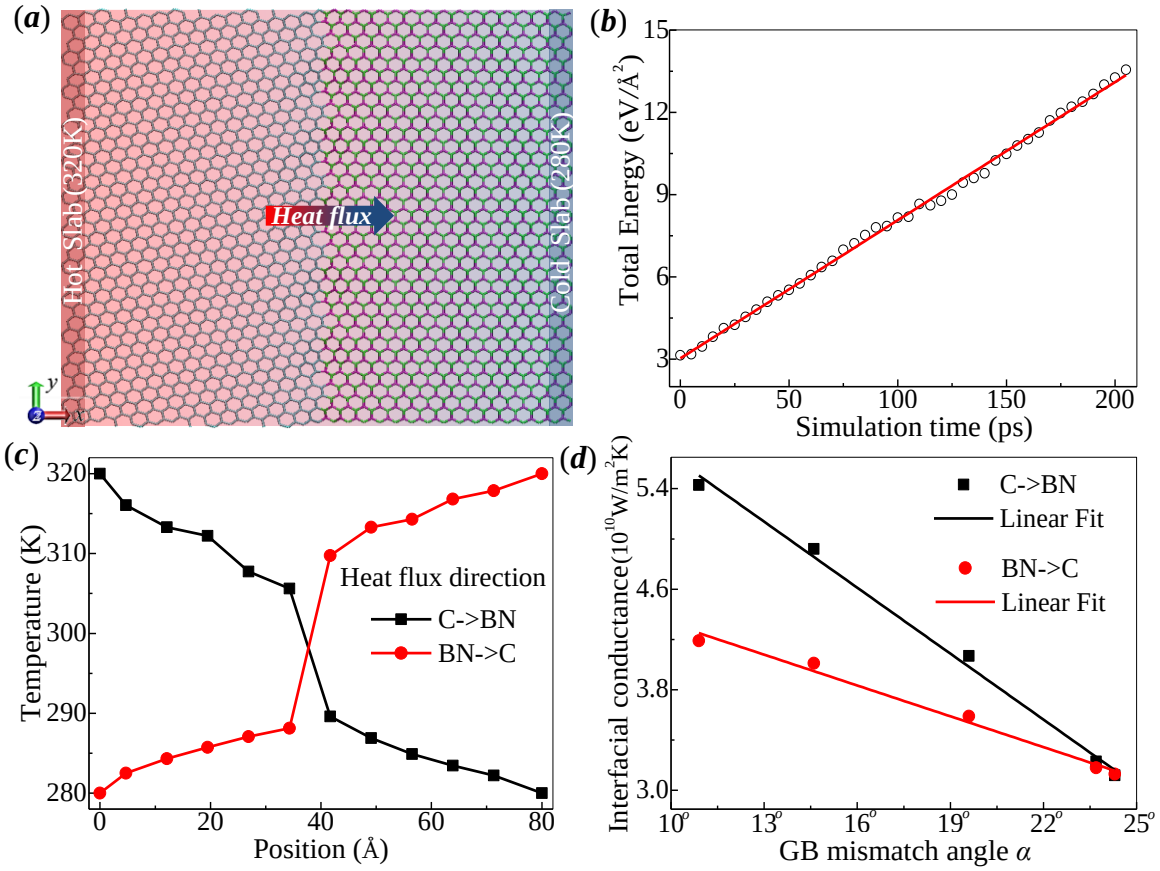

Fig. 5. Effects of GB on the thermal transport efficiency of planar graphene/h-BN heterostructure. (***a***) Illustration of the NEMD simulation for heterostructure of graphene and h-BN embedded with hybrid GB. (***b***) Evolution of total energy transported across the nanosheet per unit cross-sectional area over simulation time. (***c-d***) Comparisons between temperature profile as well as Interfacial conductance of asymmetric GB under heat flux from graphene to h-BN and that of GB under opposite heat flux.

GBs have been revealed to affect not only the mechanical properties of polycrystalline nanomaterials but also the thermal properties. Based on the molecular dynamics simulations, we further study the dependency of thermal transport efficiency of CBN heterostructures on asymmetric GBs. We first calculate the temperature profile in heterostructure using the non-

equilibrium molecular dynamics (NEMD) method as described in simulation methodology. The black line in Fig. 5*c* shows the temperature profile of hybrid nanosheet under heat flux from graphene to h-BN. In the case of hybrid nanosheet with asymmetric GB, the temperature profiles in graphene and h-BN domains are linear while a sudden jump of temperature ΔT arises at the GB. The thermal transfer efficiency of the GB between graphene and h-BN is evaluated by the interfacial conductance (Kapitza conductance) *G*, which is determined by the equation:[52]

$$G = \frac{J}{\Delta T} \tag{8}$$

where *J* is energy transported across the interface of graphene and h-BN grains per unit cross-sectional area and unit time as defined by Eq. 2. The black line in Fig. 5*d* shows the calculated interfacial conductance of asymmetric GBs when heat transfer occurs from graphene to h-BN. It is noticeable that the interfacial conductance of GBs decreases monotonically with the mismatch angles of GBs. The deterioration of interfacial conductance with mismatch angle can be qualitatively interpreted by the density of 5-7 defects along GB. As mismatch angle α increases, the hybrid GB has larger density of the 5-7 defects which act as phonon scattering centers during the thermal transport. The increase of GB density results in more phonon scatterings, which lead to the drop of interfacial conductance. As a consequence, the hybrid GB possesses a lower interfacial conductance when the mismatch angle becomes larger.

We further consider the effect of GB on thermal transfer efficiency, which is found sensitive to the direction of heat flux. The transfer efficiency of heat flux from graphene to h-BN is different from that of heat flux from h-BN to graphene. The temperature profile of GB (4,2)|(3,3) under thermal flux from h-BN to graphene are plotted by the red curve in Fig. 5*c* for comparison. It is noticeable that the temperature drop ΔT is larger when heat transfers across

the GB from h-BN to graphene under the same temperature gradient. Fig. 5*d* further shows the comparison between interfacial conductance of GB for opposite directions of thermal flux. The transfer efficiency of CBN hybrid GBs from graphene to h-BN is always higher than that for the opposite direction. Such asymmetric interfacial conductance suggests a crucial thermal rectification at the interface between graphene and h-BN grains. In fact, thermal rectification has been observed in asymmetric graphene nanoribbon experimentally[53] and theoretically[54]. Many nanoscale systems are also reported to have high thermal rectification factor by molecular dynamics simulations, including graphene Y-junction [55], and surface functionalized graphene[56]. In our simulations, the thermal rectification factor of asymmetric CBN GB is up to 15%, which is higher than the reported rectification factor of asymmetric graphene GB[57]. Such thermal rectification of hybrid GB provides a possible design of planar heterogeneous sheet-based thermal rectifier for the control of heat flux at nanoscale.

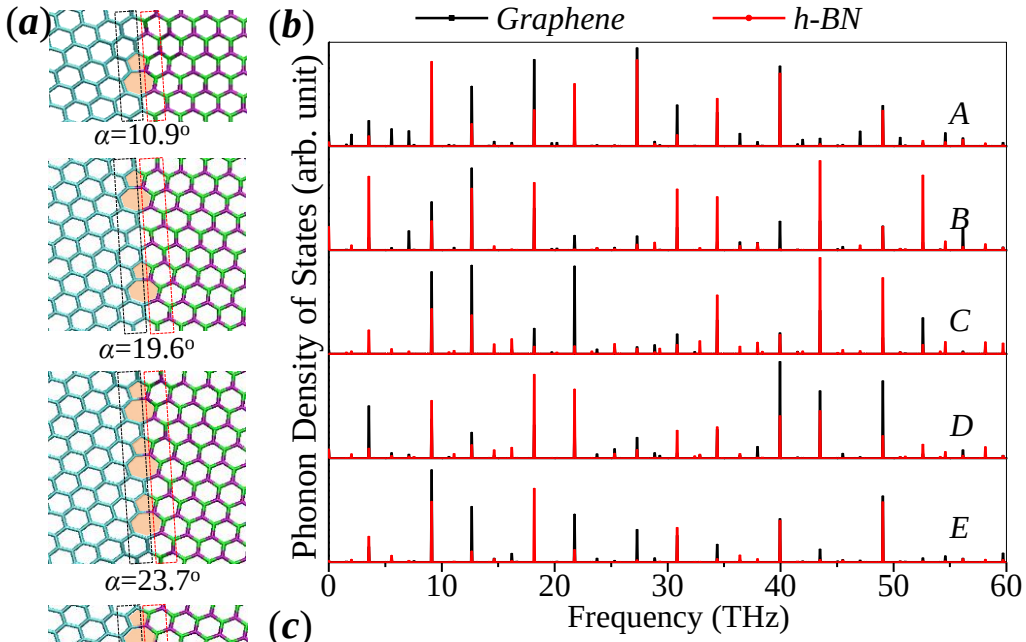

(c)

	A	*B*	*C*	*D*	*E*
α	10.9°	14.6°	19.6°	23.7°	24.3°
PDOS overlap	0.0136	0.0123	0.0113	0.0104	0.0102

Fig. 6 Phonon density of states for the interfacial atoms at the GB of graphene (black box) and h-BN (red box).

In order to interpret the mismatch angle-dependence of interfacial conductance more accurately, we carry out detailed analysis for the phonon density of states (PDOS) for interfacial atoms of GB. From lattice dynamic point of view, the phonon transport across the interface between two joining materials is strongly dependent on the overlap of phonon density of states (PDOS) between them. The PDOS overlap between the interfacial atoms which belonging to the adjacent graphene and h-BN grains is responsible for the interfacial thermal conductance of GB. A high PDOS overlap between the interfacial atoms of two materials indicates that the phonons pass through the interface more easily, i.e., a high interfacial conductance. For the hybrid graphene/h-BN GB, the GB atoms are divided into two groups: interfacial carbon atoms of

graphene and the interfacial atoms of h-BN. As the snapshots shown in Fig. 6*a*, the carbon atoms in black box are interfacial carbon atoms while the boron and nitride atoms in red box belongs to h-BN. The PDOS of these two groups of interfacial atoms are calculated by the Fourier transform of atom velocity autocorrelation function during equilibrium, and can be obtained by

$$D(\omega) = \int_0^{\tau} \frac{\langle v(t)v(0)\rangle}{\langle v(0)v(0)\rangle} \exp(-i\omega t)dt \tag{9}$$

where ω is the frequency, v is the velocity of carbon atoms, $\langle ... \rangle$ denotes time and atom number-averaged velocity autocorrelation function, τ is the time duration for calculation. Fig. 6*b* shows the calculated PDOS of these two groups of interfacial carbon atoms (black line) and boron nitride atoms in GBs with different mismatch angle. It's noticed that carbon atoms and boron-nitride atoms at the interface have a mismatch in PDOS. To quantify the overlap of PDOS, we define the value of overlap (S) as

$$S = \frac{\int_0^{\infty} D_1(w)D_2(w)dw}{\int_0^{\infty} D_1(w)dw \int_0^{\infty} D_2(w)dw} \tag{10}$$

where $D_1(w)$, $D_2(w)$ represent the PDOS of two groups of interfacial atoms C and BN, separately. The calculated overlap S for each group of PDOS between interfacial C atoms and BN atoms are listed in tables of Fig. 6*c*. Between the considered five groups of hybrid GBs, the GB with mismatch angle α = 10.9^o has the highest PDOS overlaps S, and the overlap decreases with the increase of mismatch angle. Such comparison indicates that GBs with large mismatch angle have the lowest interfacial thermal resistance than that of GBs with small mismatch angle, which is consistent with the described interfacial conductance in Fig. 5*d*. Further studies on the dependency of thermal conductance on orientation of GBs embedded in planar heterostructures are expected.

Conclusions

In conclusion, we have studied the mechanical and thermal properties of GB in planar heterostructure of graphene and h-BN. The strength of polycrystalline heterostructure has been demonstrated to be governed by the asymmetric GB connecting graphene and h-BN grains. The mechanical and thermal properties of asymmetric GB are found sensitive to the mismatch angle between the chirality of graphene and h-BN grains. With the increase of mismatch angle, the strength of GB increase anomalously with the density of 5-7 defects due to the interaction between polarized stress fields of 5-7 defects. By idealizing the 5-7 defects as a pair of adjacent positive and negative disclination cores, the stress field of asymmetric GB is successfully derived using the classical disclination theory. The derived theoretical field not only agrees well with the MD simulation but also provide insight into the anomalous mechanical property of GB. The theoretical intrinsic stress of GB caused by the lattice mismatch show that the stress distribution becomes more uniform under large mismatch angle. Decrease of stress concentration under applied tension results in the improvement of ultimate strength and strain. The asymmetric hybrid GB is also found to affect the thermal transport efficiency when heat flows across the GB. By comparing the interfacial conductance of GB for opposite direction of heat flux, it is observed that the efficiency of heat transport from graphene to h-BN is higher than that from h-BN to graphene. Such thermal rectification suggests that planar heterostructure has potential application for thermal control at nanoscale.

Conflicts of interest

There are no conflicts to declare.

Acknowledgement

We gratefully acknowledge the support provided by the National Natural Science Foundation of China (No. 11402145) and the Open Fund of State Key Laboratory of Information Photonics and Optical Communications (Beijing University of Posts and Telecommunications), P. R. China. Y. Li also acknowledge the support of the Medical-Engineering Cross Fund of Shanghai Jiao Tong University (YG2015MS13, YG2017QN64). The computational support for this study was provided by the Center for HPC, Shanghai Jiao Tong University.

References

1. R. S. Krsmanović and Ž. Šljivančanin, *The Journal of Physical Chemistry C*, 2014, **118**, 16104-16112.
2. M. Kan, Y. Li and Q. Sun, *Wiley Interdisciplinary Reviews: Computational Molecular Science*, 2016, **6**, 65-82.
3. D. Golberg, P. M. F. J. Costa, O. Lourie, M. Mitome, X. Bai, K. Kurashima, C. Zhi, C. Tang and Y. Bando, *Nano Lett.*, 2007, **7**, 2146-2151.
4. Y. Chen, J. Zou, S. J. Campbell and G. Le Caer, *Appl. Phys. Lett.*, 2004, **84**, 2430-2432.
5. N. Sai and E. J. Mele, *Phy. Rev. B*, 2003, **68**, 241405.
6. A. C. Neto, F. Guinea, N. Peres, K. S. Novoselov and A. K. Geim, *Rev. Mod. Phys.*, 2009, **81**, 109.
7. Z. Zhang and W. Guo, *Phy. Rev. B*, 2008, **77**, 075403.
8. L. Jiang and W. Guo, *J. Mech. Phys. Solids*, 2011, **59**, 1204-1213.
9. K. Watanabe, T. Taniguchi and H. Kanda, *Nature materials*, 2004, **3**, 404-409.
10. J. Jung, Z. Qiao, Q. Niu and A. H. MacDonald, *Nano Lett.*, 2012, **12**, 2936-2940.
11. J. da Rocha Martins and H. Chacham, *ACS nano*, 2010, **5**, 385-393.
12. Y. Li, D. Datta and Z. Li, *Carbon*, 2015, **90**, 234-241.
13. B. Xu, Y. H. Lu, Y. P. Feng and J. Y. Lin, *J. Appl. Phys.*, 2010, **108**, 073711.
14. H. Park, A. Wadehra, J. W. Wilkins and A. H. Castro Neto, *Appl. Phys. Lett.*, 2012, **100**, 253115.
15. J. Li and V. B. Shenoy, *Appl. Phys. Lett.*, 2011, **98**, 013105.
16. K. Yang, Y. Chen, R. D'Agosta, Y. Xie, J. Zhong and A. Rubio, *Phy. Rev. B*, 2012, **86**, 045425.
17. S. Zhao and J. Xue, *J. Phys. D: Appl. Phys.*, 2013, **46**, 135303.
18. Q. Peng, A. R. Zamiri, W. Ji and S. De, *AcMec*, 2012, **223**, 2591-2596.
19. L. Ci, L. Song, C. Jin, D. Jariwala, D. Wu, Y. Li, A. Srivastava, Z. F. Wang, K. Storr, L. Balicas, F. Liu and P. M. Ajayan, *Nat Mater*, 2010, **9**, 430-435.
20. L. Song, Z. Liu, A. L. M. Reddy, N. T. Narayanan, J. Taha-Tijerina, J. Peng, G. Gao, J. Lou, R. Vajtai and P. M. Ajayan, *Adv. Mater.*, 2012, **24**, 4878-4895.
21. C.-K. Chang, S. Kataria, C.-C. Kuo, A. Ganguly, B.-Y. Wang, J.-Y. Hwang, K.-J. Huang, W.-H. Yang, S.-B. Wang, C.-H. Chuang, M. Chen, C.-I. Huang, W.-F. Pong, K.-J. Song, S.-J. Chang, J.-H. Guo, Y. Tai, M. Tsujimoto, S. Isoda, C.-W. Chen, L.-C. Chen and K.-H. Chen, *ACS Nano*, 2013, **7**, 1333-1341.
22. Y. Gao, Y. Zhang, P. Chen, Y. Li, M. Liu, T. Gao, D. Ma, Y. Chen, Z. Cheng, X. Qiu, W. Duan and Z. Liu, *Nano Lett.*, 2013, **13**, 3439-3443.
23. L. Ci, L. Song, C. Jin, D. Jariwala, D. Wu, Y. Li, A. Srivastava, Z. Wang, K. Storr and L. Balicas, *Nature materials*, 2010, **9**, 430-435.
24. Z. Liu, L. Ma, G. Shi, W. Zhou, Y. Gong, S. Lei, X. Yang, J. Zhang, J. Yu, K. P. Hackenberg, A. Babakhani, J.-C. Idrobo, R. Vajtai, J. Lou and P. M. Ajayan, *Nature Nanotechnol.*, 2013, **8**, 119-124.

25. K. Choy, *Prog. Mater Sci.*, 2003, **48**, 57-170.
26. J. J. Tietjen, *Annu. Rev. Mater. Sci.*, 1973, **3**, 317-326.
27. L. Liu, J. Park, D. A. Siegel, K. F. McCarty, K. W. Clark, W. Deng, L. Basile, J. C. Idrobo, A.-P. Li and G. Gu, *Science*, 2014, **343**, 163-167.
28. B. Mortazavi and G. Cuniberti, *RSC Advances*, 2014, **4**, 19137-19143.
29. K. Kim, Z. Lee, W. Regan, C. Kisielowski, M. Crommie and A. Zettl, *ACS nano*, 2011, **5**, 2142-2146.
30. P. Y. Huang, C. S. Ruiz-Vargas, A. M. van der Zande, W. S. Whitney, M. P. Levendorf, J. W. Kevek, S. Garg, J. S. Alden, C. J. Hustedt and Y. Zhu, *Nature*, 2011, **469**, 389-392.
31. A. L. Gibb, N. Alem, J.-H. Chen, K. J. Erickson, J. Ciston, A. Gautam, M. Linck and A. Zettl, *J. Am. Chem. Soc.*, 2013, **135**, 6758-6761.
32. A. Cao and Y. Yuan, *Appl. Phys. Lett.*, 2012, **100**, 211912.
33. J. Xiao, J. Staniszewski and J. Gillespie, *Materials Science and Engineering: A*, 2010, **527**, 715-723.
34. H. I. Rasool, C. Ophus, W. S. Klug, A. Zettl and J. K. Gimzewski, *Nature communications*, 2013, **4**.
35. Y. Wei, J. Wu, H. Yin, X. Shi, R. Yang and M. Dresselhaus, *Nature materials*, 2012, **11**, 759-763.
36. R. Grantab, V. B. Shenoy and R. S. Ruoff, *Science*, 2010, **330**, 946-948.
37. Y. Wei, J. Wu, H. Yin, X. Shi, R. Yang and M. Dresselhaus, *Nat Mater*, 2012, **11**, 759-763.
38. A. Wei, Y. Li, D. Datta, H. Guo and Z. Lv, *Comp. Mater. Sci.*, 2017, **126**, 474-478.
39. Z. Shijun and X. Jianming, *J. Phys. D: Appl. Phys.*, 2013, **46**, 135303.
40. N. Ding, X. Chen and C.-M. L. Wu, *Sci. Rep.*, 2016, **6**, 31499.
41. Z. Zhang, Y. Yang and B. I. Yakobson, *J. Mech. Phys. Solids*, 2014, **70**, 62-70.
42. B. Yang, H. Xu, J. Lu and K. P. Loh, *J. Am. Chem. Soc.*, 2014, **136**, 12041-12046.
43. A. Kınacı, J. B. Haskins, C. Sevik and T. Çağın, *Physical Review B*, 2012, **86**, 115410.
44. S. Plimpton, *J. Comput. Phys.*, 1995, **117** 1-19.
45. Z. Basinski, M. Duesbery and R. Taylor, *Can. J. Phys.*, 1971, **49**, 2160-2180.
46. N. Chandra, S. Namilae and C. Shet, *Phy. Rev. B*, 2004, **69**, 094101.
47. B. Mortazavi and S. Ahzi, *Carbon*, 2013, **63**, 460-470.
48. R. Abadi, R. P. Uma, M. Izadifar and T. Rabczuk, *Comp. Mater. Sci.*, 2016, **123**, 277-286.
49. J. Wu and Y. Wei, *J. Mech. Phys. Solids*, 2013, **61**, 1421-1432.
50. J. D. Eshelby, *Br. J. Appl. Phys.*, 1966, **17**, 1131.
51. J. C. M. Li, *Surf. Sci.*, 1972, **31**, 12-26.
52. A. Bagri, S.-P. Kim, R. S. Ruoff and V. B. Shenoy, *Nano Lett.*, 2011, **11**, 3917-3921.
53. H. Wang, S. Hu, K. Takahashi, X. Zhang, H. Takamatsu and J. Chen, 2017, **8**, 15843.
54. J. Hu, X. Ruan and Y. P. Chen, *Nano Lett.*, 2009, **9**, 2730-2735.
55. G. Zhang and H. Zhang, *Nanoscale*, 2011, **3**, 4604-4607.
56. Y. Li, A. Wei and D. Datta, *Carbon*, 2017, **113**, 274-282.
57. H.-Y. Cao, H. Xiang and X.-G. Gong, *Solid State Commun.*, 2012, **152**, 1807-1810.

Supplementary information

Mechanical and thermal properties of grain boundary in planar heterostructure of graphene and hexagonal boron nitride

Yinfeng Li[a,b,*], Anran Wei [a], Haimin Yao[c]

a. Department of Engineering Mechanics, School of Naval Architecture, Ocean and Civil Engineering (State Key Laboratory of Ocean Engineering), Shanghai Jiao Tong University, Shanghai 200240, China

b. Collaborative Innovation Center for Advanced Ship and Deep-Sea Exploration, Shanghai 200240, China

c. Department of Mechanical Engineering, The Hong Kong Polytechnic University, Hong Kong, China

Video S1 Dynamic failure process of symmetric GB (4,2)|(3,3) under uniaxial tension along *x*-direction

Video S2 Dynamic failure process of symmetric GB (7,3)|(6,4) under uniaxial tension along *x*-direction

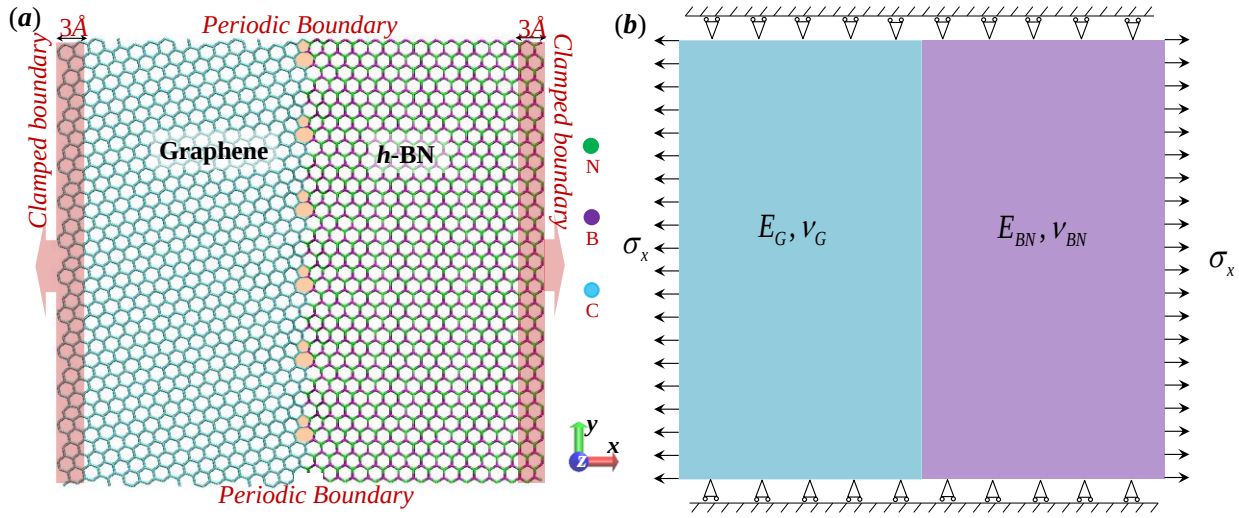

Fig. S1 Illustration for the modelling of hybrid graphene/h-BN nanosheet under uniaxial tension along horizontal direction and periodic boundary condition along top and bottom direction. (***a***) shows the atomistic model for MD simulations, and (***b***) is the continuum model for the theoretical analysis based on classical disclination theory.